AIAA SciTech Forum
6-10 January 2025, Orlando, FL
AIAA SCITECH 2025 Forum

10.2514/6.2025-2753

Statistics of a turbulent boundary layer under a favorable-adverse pressure gradient sequence

Aman Agrawal*, Theresa Saxton-Fox†
University of Illinois at Urbana-Champaign, Champaign, IL 61820

A statically deformable ceiling was used at the Turbulence Dynamic Research facility at the University of Illinois at Urbana-Champaign. This facility was used to impose static spatially varying pressure gradients in a favorable-adverse (FAPG) arrangement. This study focuses on the FPG region of this flowfield which experiences a rapid spatial variation of its pressure gradient over 6.2δ. Non-time-resolved particle imaging velocimetry data were captured for 6 pressure gradients and 6 Reynolds numbers. This manuscript focuses on $Re_\tau = 953$ and four pressure gradient cases that have maximum acceleration parameters of $K_{max} \times 10^6$ = 0, 2.43, 4.77, and 5.97. The Reynolds stresses and turbulent kinetic energy of the boundary layer were investigated. The results were analyzed for the occurrence of relaminarization and it was concluded that no relaminarization occurred in any of the cases. The Reynolds stresses showed behavior suggestive of an internal layer, including knee points in $\overline{u'u'}$. However, no conclusive evidence was found to support this hypothesis.

I. Nomenclature

PG	=	pressure gradient
TBL	=	turbulent boundary layer
FPG	=	favorable pressure gradient
APG	=	adverse pressure gradient
FAPG	=	favorable-adverse pressure gradient sequence
ZPG	=	zero pressure gradient
K	=	acceleration parameter
ν	=	kinematic viscosity
u	=	instantaneous streamwise velocity
U	=	time-averaged streamwise velocity
u_{rms}	=	RMS of instantaneous streamwise velocity
u'	=	$u - U$
U_e	=	edge velocity
β	=	Clauser pressure gradient parameter
δ^*	=	displacement thickness
τ_w	=	wall shear stress
δ	=	boundary layer thickness
Re	=	Reynolds number
Re_τ	=	friction Reynolds number
β_0	=	Clauser pressure gradient parameter calculated using ZPG parameters
L	=	half length of ceiling (length of FPG application)
y^+	=	inner-scaled y-coordinate
$\frac{\overline{u'u'}}{U_e^2}$	=	uu Reynolds stress
$\frac{\overline{v'v'}}{U_e^2}$	=	vv Reynolds stress
$\frac{\overline{u'v'}}{U_e^2}$	=	uv Reynolds stress
RS	=	Reynolds stress
H	=	shape factor
δ^*	=	displacement thickness

*PhD Student, Aerospace Engineering, Grainger College of Engineering, 104 S Wright St, Urbana, Illinois 61820, AIAA Student Member.
†Assistant Professor, Aerospace Engineering, Grainger College of Engineering, 104 S Wright St, Urbana, Illinois 61820, AIAA Member.

θ = momentum thickness
η = threshold for boundary layer edge detection

II. Introduction

Turbulent boundary layers under pressure gradients have been a consistent focus of research for the past decades, due to their relevance to many aerospace applications. PG flows show a departure from the canonical structure of the mean profile of a TBL under a ZPG. This departure from the canonical structure of a boundary layer is characterized by the strength of the PG as well as the accumulated PG or PG history. The strength of a pressure gradient is commonly represented by the acceleration parameter, $K \equiv \frac{\nu}{U_e^2}\frac{dU_e}{dx}$, or the Clauser pressure gradient parameter, $\beta \equiv \frac{\delta^*}{\tau_w}\frac{dP}{dx}$.

Under a constant FPG applied immediately downstream of a ZPG, the TBL becomes thinner with an enlargement (by percentage) of the viscous sublayer and buffer regions, as well as a thinning of the logarithmic region. For mild FPGs ($K < 0.5 \times 10^-6$), this presents as a slight thinning of the log region [1], whereas, for moderate-strong FPGs ($0.5 \times 10^{-6} < K < 6 \times 10^{-6}$), this presents as an absence or severe alteration of the log region [2–4]. The Reynolds stresses also show a decay, primarily in the outer region due to the reduction in turbulent production brought about by the influence of the PG, and the wake disappears [4]. Under an APG applied immediately after a ZPG, the TBL experiences nearly the opposite behavior. The BL grows thicker, the viscous sublayer and buffer regions become thinner, and the log region is thicker. The log region shows a significant departure from canonical ZPG behavior, especially large and apparent when $\beta > 2$ [5]. Besides the strength of local PGs, TBLs have also shown a dependence on upstream conditions. This has been referred to as "history effects" within recent literature [6]. Vinuesa et al. [6] characterize 11 APG TBL datasets, all exhibiting different flow histories.

There is a need for turbulence models that can predict the behavior of TBLs under the influence of PGs, to accurately predict separation, skin friction, and heat transfer. Pressure gradient flows with a simple history, i.e., flows which experience a single PG condition applied to an incoming ZPG and held for a long streamwise extent have been studied extensively in both experiments [1, 2, 4, 7–10] and simulations [11–15]. This type of flowfield is modeled well by low-order RANS (Reynolds-averaged Navier-Stokes) turbulence models like the Spalart-Allmaras and the $k-\omega$ models [16–18]. However, recent studies, including Balin and Jansen [19], have shown that low-order RANS models are ineffective for geometries like bump flows, which impose a complex pressure gradient history. These models are ineffective in scenarios with large spatial variations of pressure gradients or sign reversals.

The types of PG histories with large spatial variations of pressure gradients and/or sign reversals are an especially interesting area of study. The PG strength generally varies significantly over a relatively small streamwise extent, with regions of strong and weak pressure gradients. The spatial variation in strength as well as the local PG can affect the response of the flow. Additionally, the bump geometry has a transition from a strong favorable pressure gradient to a strong adverse pressure gradient, two PG configurations that show essentially opposing behavior. The behavior of flow over a bump has been studied for decades, and there are several studies now on pressure gradients that vary spatially, including with sign changes and curvature changes [19–24]. These studies [19, 23, 24] show a quicker deviation from canonical in comparison to either pure APG or FPG flows. They [19, 23, 24] have also shown the presence of multiple humps or knee points in the Reynolds stress profiles for these flows. These studies were performed on a geometric configuration where the boundary layer was investigated over a smooth bump. The upside-down configuration of this geometry, where the turbulent boundary layer is investigated over the flat plate under the pressure gradient applied by a bump geometry, is also of interest. This type of flowfield will be referred to as a favorable-adverse pressure gradient or, FAPG, due to the spatial arrangement of the two pressure gradients, namely favorable followed by adverse. The work of Parthasarathy and Saxton-Fox [22], conducted in the same facility and flowfield as this work, is of particular interest.

In their work, [22] investigated the APG region of the flowfield under several steady as well as unsteady pressure gradient configurations. They discovered the presence of an internal layer within this region [22]. This internal layer was characterized by plotting the velocity, U/U_e against $\sqrt{y/\delta}$. The edge of the internal layer presents as a kink in the velocity profile following two intersecting lines. The study observed a bifurcation between the internal layer and the remaining boundary layer, where the internal layer became “active” and the remaining boundary layer, or outer region, became “passive.” Here, becoming passive refers to the lack of production of turbulent kinetic energy in this outer region, where TKE production remains suppressed as a result of the FPG application. The internal layer on the other hand becomes “active,” referring to the spike in production of TKE as characteristic of an APG TBL.

This work is interested in investigating the FPG region of this flowfield, where a rapid spatially changing FPG is applied to an incoming ZPG TBL. Accordingly, this work evaluates and presents the statistics within the FPG region of interest for this flowfield.

III. Experiment

A. Wind tunnel, test conditions, and setup

This experiment was performed at the Turbulent Boundary Layer Wind Tunnel Facility located in the Aerodynamics Research Laboratory at the University of Illinois as pictured in figure 1. Dormant air enters the wind tunnel through a 10.19 cm thick honeycomb straightener. This air then passes through four layers of turbulence-reducing mesh, followed by a 24:1 contraction ratio inlet. The air then enters the test section, which is $0.381m \times 0.381m \times 3.687m$ or 15" × 15" × 12′. The freestream turbulence intensity in the test section is $\approx 1\%$. A flat plate is introduced at the beginning of the test section, featuring a strip of sandpaper at the leading edge to act as a trip. The test area is located $2.3m$ downstream of the leading edge. The zero pressure gradient 99.5% boundary layer thickness, δ, at the test area was $44mm$. Measurements were made at six friction Reynolds numbers, Re_τ, of which this paper focuses on $Re_\tau = 950$.

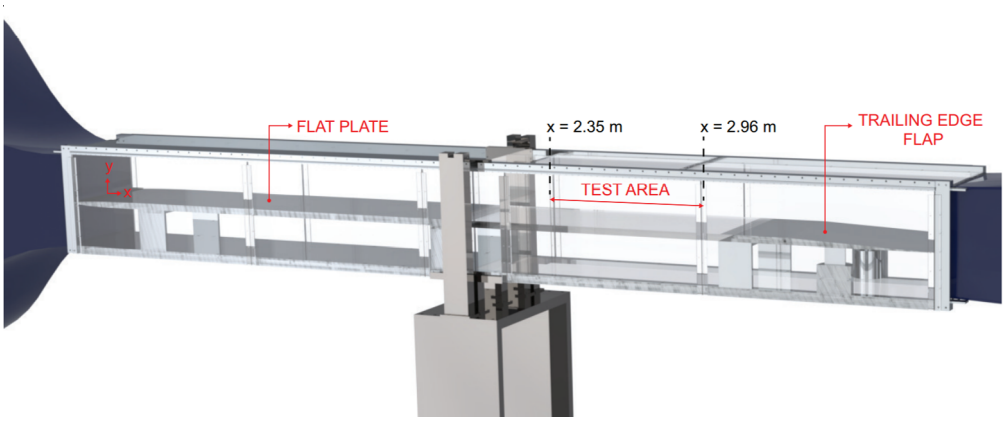

Fig. 1 Schematic of the wind tunnel facility, including the x-location of the test section with reference, $x = 0$, at the leading edge of the flat plate [25]

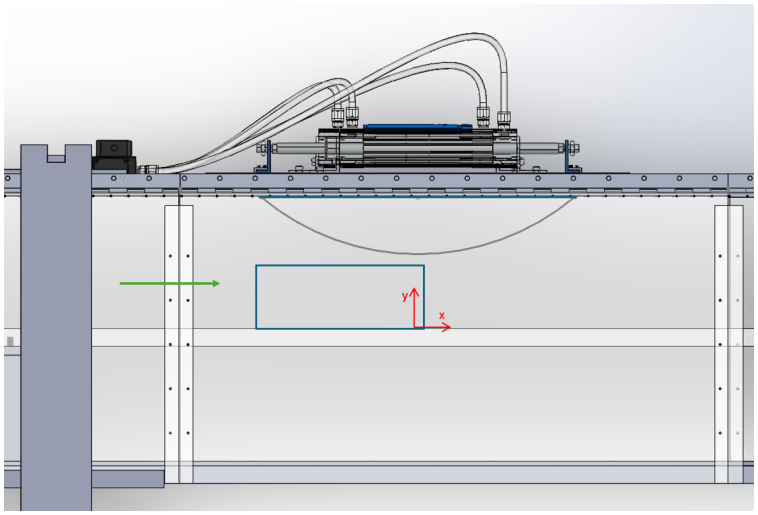

Fig. 2 Flexible ceiling panel used to apply the spatial FAPG within the test area. The green arrow indicates the flow direction and the blue box shows the field of view within which data were collected

A flexible ceiling panel is used to apply a favorable-adverse pressure gradient over the test area. This assembly can be used to apply continuously varying as well as unsteady pressure gradients. However, this experiment focuses on steady pressure gradients. The acceleration parameter, K, and Clauser PG parameter, β_0, are presented in figure 3. β_0 is $\beta_0 = \left(\frac{\delta^*}{\tau_w}\right)_{zpg} \frac{dP}{dx}$, the Clauser PG parameter calculated using the ZPG values of δ^* and τ_w. At present, we will focus

on the four PG cases detailed in table 1. Note that the pressure gradients shown in figure 3 extend further downstream up to $x/L = 1.0$, however, the flow separates from the ceiling just downstream of $x/L = 0.8$ and the subsequent pressure distribution flattens out [25]. The FPG is applied over the length of $\approx 6.2\delta_0$, where δ_0 is the ZPG Boundary layer thickness.

Side-by-side Planar PIV (particle image velocimetry) was performed in a streamwise wall-normal plane located at the centerline of the tunnel. The field of view for this was $242mm \times 92mm$, or $6.5\delta \times 2.5\delta$. The imaging was performed using a Phantom VEO710L and a Photron Fastcam Nova S6, with a spatial resolution of 2.6 vectors/mm (115 vectors/δ_{ZPG}, and $\delta^+_{ZPG} = 7.2$). Data were sampled at a sampling rate of $100Hz$. 11000 snapshots were collected for six Reynolds numbers and 6 pressure gradients. The closest data point to the wall was collected at $y^+ = 60$. This is limited by near-wall laser impingement. This paper focuses on the cases described in table 1. A Terra PIV 527-80-M dual-pulse laser was used along with suitable sheet-forming optics to generate a laser sheet passing through the plane of interest. The laser-camera timing was handled by a Lavision programmable timing unit in conjunction with Davis 10.2. A mineral-oil-based smoke was introduced at the inlet of the tunnel to act as the seeding.

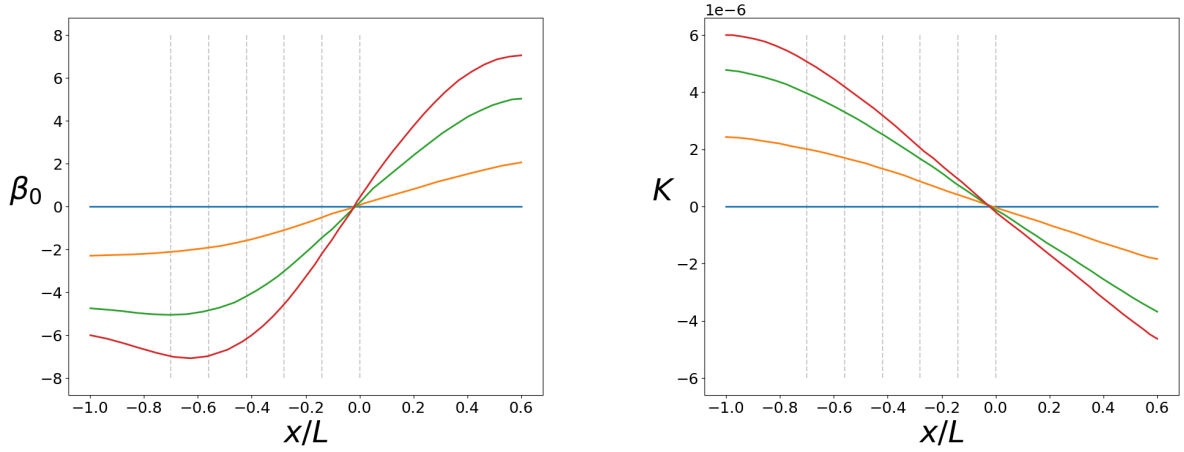

(a) Clauser pressure gradient parameter, β_0 **(b) Acceleration parameter, K**

Fig. 3 Pressure gradient parameters applied by the flexible ceiling, calculated using a conservation of mass approach and verified by pressure taps to be within 2% [25]. Grey dashed lines indicate the streamwise locations we look at.

Case Name	Color	Re_τ	$\delta_0(m)$	$K_{max} \times 10^6$	$\beta_{0,max}$
PG0	Blue	953	0.044	$\simeq 0$	$\simeq 0$
PG8	Orange	953	0.044	2.4286	-2.2990
PG16	Green	953	0.044	4.7657	-5.0641
PG21	Red	953	0.044	5.9733	-7.0709

Table 1 Relevant parameters for cases investigated

B. Boundary layer edge detection

Boundary layer edge detection for ZPG flows is well understood and uses a definition of $U(\delta)/U_\infty = 0.99$, typically referred to as δ_{99}. This definition is unsuitable for pressure gradient flows as we see non-zero $\partial U/\partial y$ in the freestream. There are several proposed methods in the literature that attempt to define an equivalent for PG flows. We tried several common techniques proposed, such as the diagnostic plot technique [6], the $-y\Omega_z$ method [26, 27], and a shear threshold method [16].

The diagnostic plot technique is based on a diagnostic parameter $u_{rms}/U\sqrt{H}$, where $H = \delta^*/\theta$, corresponding to a value of 0.02 at δ_{99} consistently for multiple Reynolds numbers and pressure gradients [6]. However, Based on observations when implemented to our data, this technique is susceptible to noise in the freestream velocity data which can be compensated for by increasing the target threshold, but leads to inconsistent boundary layer edge detection. A lot of other people have found success using this technique, but it did not work for our dataset.

The shear threshold method relies on the fact that the Reynolds shear stress, $\overline{u'v'}/U_e^2$ approaches 0 at the edge of the boundary layer [16]. The method uses a threshold on the value of the Reynolds shear stress that is a fraction of the maximum Reynolds shear stress observed in the field. In particular, they specify a $5\% \max(\overline{u'v'}/U_e^2)$ threshold [16]. This technique relies on resolving the peak of $\overline{u'v'}$, which occurs in the near-wall region. In our PIV data, surface reflections corrupt and prevent full measurement of this peak. This would still be usable by adjusting the threshold parameter if the fraction of the non-measured boundary layer was consistent, but due to the different application of pressure gradients, the fraction of the boundary layer with missing measurements is different, leading to inconsistent edge detection when this technique is used for our experimental data.

The $-y\Omega_z$ method uses the vorticity parameter,

$$-y\Omega_z = -y\left(\frac{\partial V}{\partial x} - \frac{\partial U}{\partial y}\right). \tag{1}$$

$-y\Omega_z$ approaches 0 at the edge of the boundary layer, using a $2\% \max(-y\Omega_z)$ [27] and unlike the shear threshold has a peak farther away from the wall. However, the need for derivatives, especially $\partial V/\partial x$, is challenging for experimental data. This method tends to amplify the noise present in the data, even when a filter or convolution is used. In some conditions the freestream vorticity is higher than the threshold, meaning that the threshold is never achieved, and thus the boundary layer edge is never found.

We provide here an alternative boundary layer edge detection method, taking elements from the three techniques described, that we found to be more robust to experimental noise. We take the threshold definition approach from DPT, using $\overline{u'v'}$ as our primary metric for identifying the edge of the boundary layer. We call it the shear stress slope threshold method. This technique is based on the fact that the slope of $\overline{u'v'}$ approaches 0 at the edge of the boundary layer. The technique uses a Savitzky-Golay filter to calculate a smoothed derivative of $\overline{u'v'}$. The Savitzky-Golay filter is a type of convolution scheme that convolves each data point with n nearest points by best fitting a degree m polynomial using the least squares method [23]. The local derivative at each point is then the same as the derivative of the polynomial fitted, simplifying the process of obtaining the derivative. The new method avoids a definition based on a peak value, given that we may not see the peak in our measurements. For our analysis, $n = 50$ and $m = 5$ are used for the filter parameters. We then use a minimum threshold value to determine the edge of the boundary layer. The threshold value is determined

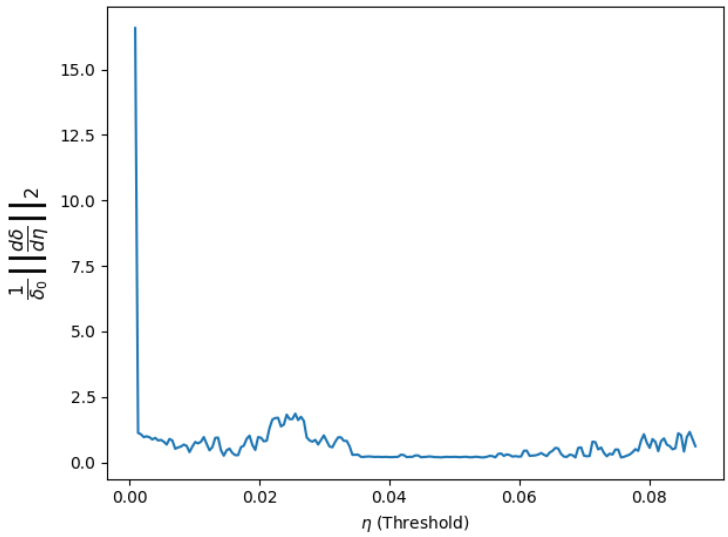

Fig. 4 The sensitivity analysis plot of the shear slope threshold for PG16

using a sensitivity analysis for each experimental dataset. We observed that the threshold is not affected by the pressure gradient applied.

Figure 4 shows the sensitivity analysis plot for the case of PG16. The sensitivity is defined as

$$\frac{1}{\delta_0}\left\|\frac{d\delta}{d\eta}\right\|_2, \tag{2}$$

where η is the threshold, and δ_0 is the ZPG boundary layer thickness using the 99.5% definition. Note that $d\delta/d\eta$ is a vector, with one entry at each streamwise location, and the 2-norm serves to compress this vector into a single term representing the sensitivity of the boundary layer edge detection to the threshold. This plot presents a large number of threshold values which are minima. We are looking for the smallest threshold in the flat region. In this case that is a value of 0.034. This value stays consistent for all pressure gradients. This threshold depends on the Reynolds number and, thus, a sensitivity analysis should be used to determine the threshold. Using the shear stress slope threshold technique, we lose some generality in its definition but allow more practical application for experimental datasets.

IV. Results and discussion

Here we present the results of our experiment and provide insights and analysis into the physics of the FAPG flowfield. The acceleration parameter K and Clauser pressure gradient parameter β_0 for these are shown in figure 3. Table 1 shows the legend for the colors in proceeding plots as well as relevant parameters for the cases discussed. Henceforth we will refer to the various pressure gradients by the case names in the table. We use edge velocity, U_e, and boundary layer thickness, δ, as our scaling units. These were identified using the technique described in section III.B.

Figures 6 and 7 show the Reynolds stresses and turbulent kinetic energy at various streamwise locations for different pressure gradient strengths. The interesting thing to note before discussing trends is that the upstream stations have a higher local pressure gradient strength but a shorter pressure gradient history or, in other words, a weaker accumulated pressure gradient. The locations where the flow is studied in figure 7 are shown schematically as grey dashed lines in figure 3.

A. Observations

Starting with individual pressure gradients, we first consider PG0. The mean velocity profile shown in figure 5 shows the expected collapse showing no significant change across the field of view, since this is a ZPG. Stronger PGs show an acceleration in the mean velocity profiles, which shows a monotonic increase with the increased strength of the PG. The Reynolds stress profiles shown in figure 6, also show some behavior consistent with a weak FPG applied to a boundary layer, especially in the range $-0.7 \leq x/L \leq -0.56$. Namely, the presence and suppression of a weak second peak in the $\overline{u'u'}$, overall suppression of the $\overline{v'v'}$, and suppression of the $\overline{u'v'}$ in the log and wake region. This behavior might be the result of a small step in the ceiling where the panel starts, or due to a small amount of deformation in the panel, but the behavior past $x/L \leq -0.56$ is consistent with a ZPG.

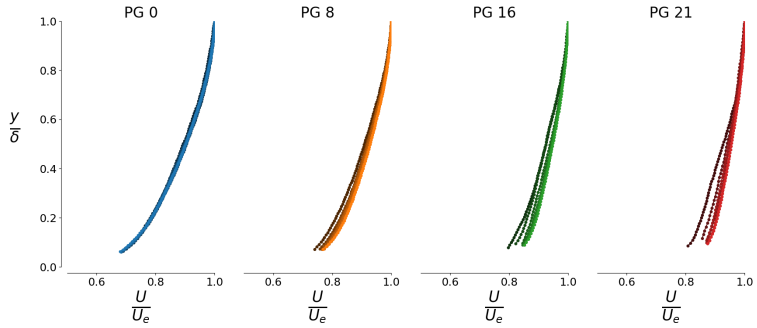

Fig. 5 Mean velocity profiles arranged by pressure gradient for the FPG region of the flowfield. Color gets lighter at downstream locations. The locations are the same ones shown in figure 7

PG8 shows a monotonic decrease in the PG strength as we move downstream, both in terms of β_0 and K, as shown in figure 3. On the first location, $x/L = -0.7$, in the $\overline{u'u'}$ (figure 6a), we expect to see a near-wall peak, which is not

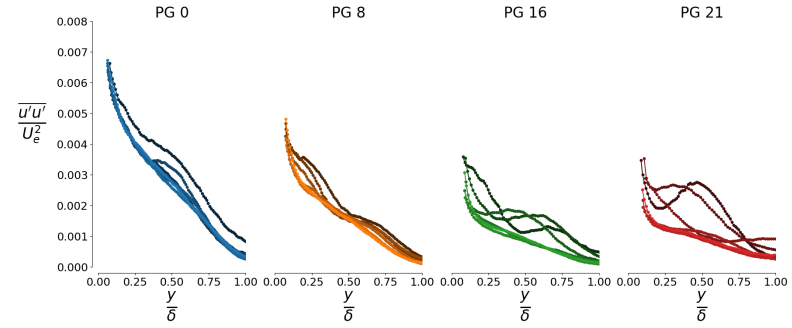

(a) Streamwise Reynolds stress

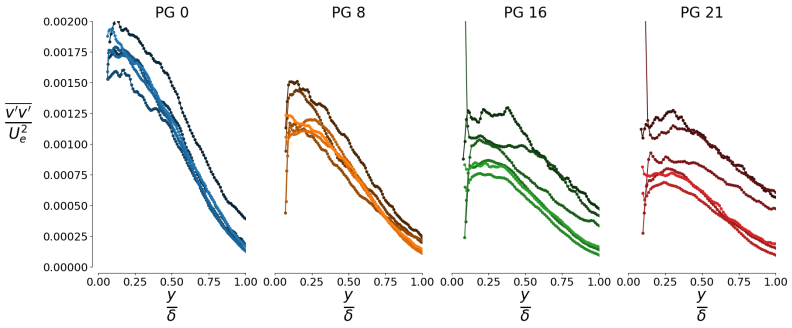

(b) Wall-normal Reynolds stress

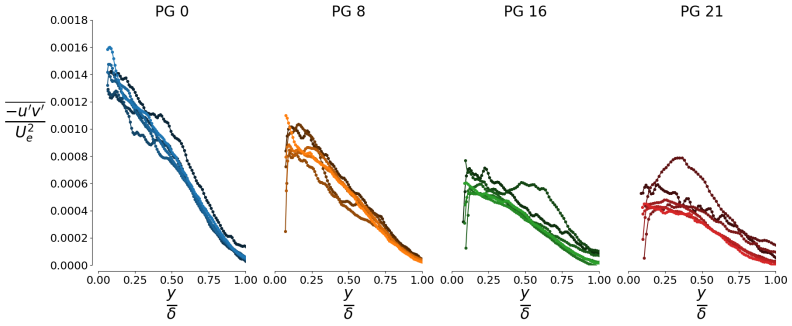

(c) Reynolds shear stress

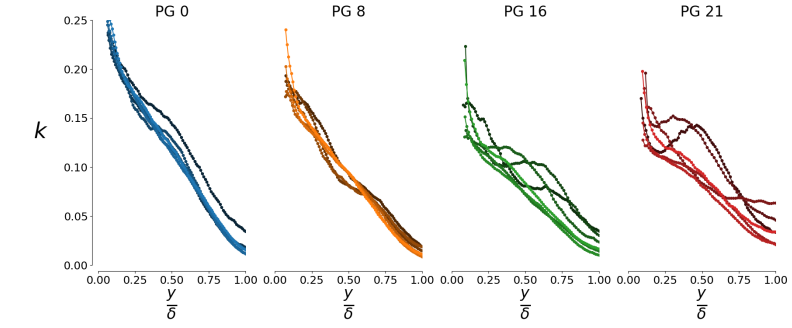

(d) Turbulent kinetic energy

Fig. 6 Reynolds stresses and turbulent kinetic energy in the FPG region of the flowfield. Color gets lighter at downstream locations. The locations are the same ones shown in figure 7

captured in our data, and we see a hump (a flatter region in the stress plot) in the log region. This behavior is consistent with a boundary layer that had previously been in a ZPG condition experiencing an FPG. As the flow moves downstream under this FPG, we see a suppression of the Reynolds stresses in the outer region. The rate of this suppression weakens as the PG weakens. This behavior is also consistent with a canonical FPG flow [4]. For the wall-normal Reynolds stresses (figure 6b), at $x/L = -0.7$, we see a peak closer to the wall with a quasi-linear decrease as we move away from the wall. As we move downstream we see an overall suppression of the Reynolds stresses. In figure 6c, at $x/L = -0.7$, $\overline{u'v'}$ has a very similar shape to that of $\overline{v'v'}$. As we move downstream we see a suppression in the log region with no significant change in the wake region. This is canonical behavior for an FPG boundary layer, and thus we similarly expect to see no change in the near-wall region. Our data do not capture this region. The turbulent kinetic energy (figure 6d) shows a near-wall peak with a monotonic decrease in TKE, showing similar behavior to the $\overline{u'u'}$. Interestingly, this shows no significant change in the overall TKE in the region captured, but does show a flattening of the energy distribution.

PG21 (figure 3) shows a monotonic decrease in strength only in terms of K. $|\beta_0|$ shows an increase in strength until it peaks at $x/L = -0.63$, and then decreases. Starting with the $\overline{u'u'}$ (figure 6a), we see a very different profile at $x/L = -0.7$ compared to that of PG8. We see the presence of a distinct second peak in the log region. As we move downstream, the second peak moves closer to the wall (and may be combining with the near-wall peak). There is no significant change in the strength of this peak. As the second peak gets closer it sees an increased $\overline{u'u'}$ into the freestream (the profile remains flat well beyond the boundary layer edge), leaving a valley in the log region. As we move downstream, this freestream $\overline{u'u'}$ value drops and the valley disappears. $\overline{v'v'}$ (figure 6b) is also a little different from that of PG8. We see a flat section at the peak instead of the more sharp peak in the previous case. We also see a much stronger suppression, as we would expect. The other feature, which is also true for PG8 but more visible here in PG21, is that the quasi-linear decrease in the log and wake regions ($y/\delta \geq 0.35$) follows a similar slope at all the locations, unlike the other two Reynolds stresses. Another feature to note here is the closeness of the RS profiles for the first two locations. These locations also happen to be on either side of the $|\beta_0|$ peak. This closeness might suggest the involvement of a physical mechanism shift or a delayed response to the PG change. Note that we do not have data upstream of $x/L = -0.7$, which would help investigate this further. $\overline{u'v'}$ (figure 6c) starts out looking very similar to the PG8 profiles at $x/L = -0.7$, but shows a very different trend. We observe a growth in the RS peaking at $y/\delta \approx 0.35$. This growth is at its maximum at $x/L \approx -0.65$, very close to the location of the $|\beta_0|$ peak. The $\overline{u'v'}$ is then suppressed in a manner consistent with canonical FPG flows [4]. We see behavior in TKE (figure 6d) very similar to the $\overline{u'u'}$. We see the formation of a second peak that moves closer to the wall, and in this case also, growing in magnitude. We see an increase in TKE levels into the free stream as well.

Finally, let's consider PG16. This PG (figure 3) shows a similar distribution to PG21 but less intense, where $|\beta_0|$ increases peaking at $x/L = -0.67$. In this case, the increase is much weaker than PG21, with an earlier peak. $\overline{u'u'}$ (figure 6a) shows behavior similar to PG21. We see the presence of a second peak at $x/L = -0.7$ that moves closer to the wall. However, in this case, the peak starts out much weaker. This peak then grows while moving closer to the wall. We note that the growth of this peak stalls out at $x/L \approx -0.55$ and remains relatively constant from there, similar to PG21 (suggesting a similar growth in PG21 happening further upstream). Looking at $\overline{v'v'}$ (figure 6b), we see similar behavior to PG21 but in this case, we see a rapid suppression in the $y/\delta < 0.5$ region just downstream of $x/L = -0.7$ $\overline{u'v'}$ (figure 6c) also shows behavior similar to PG21. However in this case the growth happens at $y/\delta \approx 0.5$ further downstream, peaking at $x/L = -0.62$. This is interesting because the $|\beta_0|$ peak happens further upstream compared to PG21. A lot of the unique trends observed happen further downstream in the PG16 case compared to the PG21 case. TKE (figure 6d) shows behavior similar to $\overline{u'u'}$ here as well.

Figure 7 provides a more effective way of comparing the 4 PGs to each other. Let's start with the $\overline{u'u'}$ (figure 7a). Here we see the similarity of the features between PG21 and PG16 but happening further upstream in PG21 compared to PG16. we see a similar secondary peak form but weaker for PG16 ($x/L = -0.42$) as compared to PG21 ($x/L = -0.56$). We see this peak move closer to the wall, and then the formation of the dip (PG16:$x/L = -0.28$, PG21:$x/L = -0.42$). We also see that the freestream $\overline{u'u'}$ increase that happens after the second and near-wall peak meet, is absent for the PG16 case compared to PG21. We also notice an almost (near-wall peak may differ) collapse for the $\overline{u'u'}$ for PG16 and PG21 between $-0.14 < x/L < 0$. We see this similarity for all the Reynolds stresses and TKE as well. Moving on to $\overline{v'v'}$ (figure 7b), we see very similar trends for both PG16 and PG21 at all locations, with the RS profiles approaching collapse at $x/L = 0$. We also see a higher RS at the boundary layer for PG16 and PG21 at the first three locations. $\overline{u'v'}$ (figure 7c) shows the production of the log region peak at $x/L = -0.56$ for both PG16 and PG21. We also notice that the RS profiles for PG16 and PG21 start to collapse in the wake region very early on and this region of collapse grows closer to the wall as we move downstream.

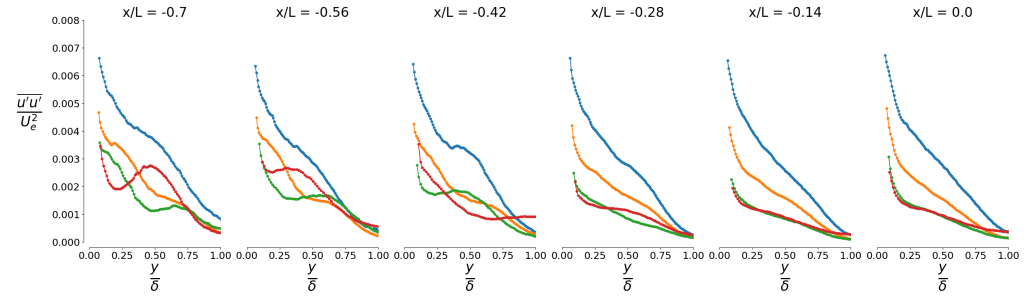

(a) Streamwise Reynolds stress

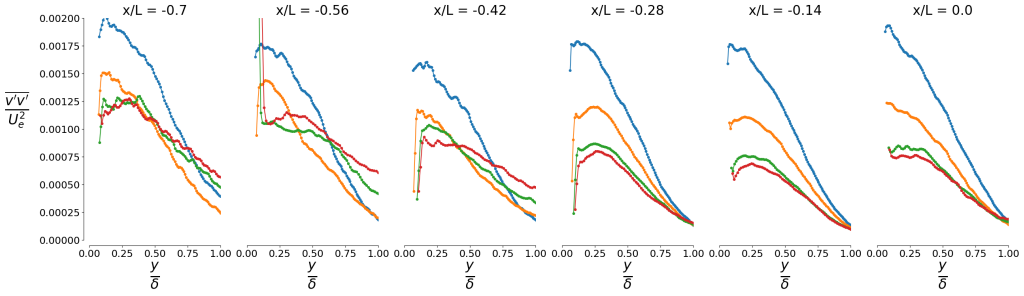

(b) Wall-normal Reynolds stress

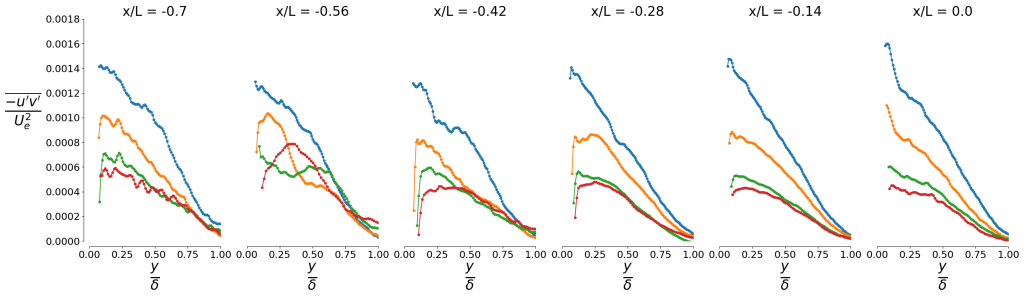

(c) Reynolds shear stress

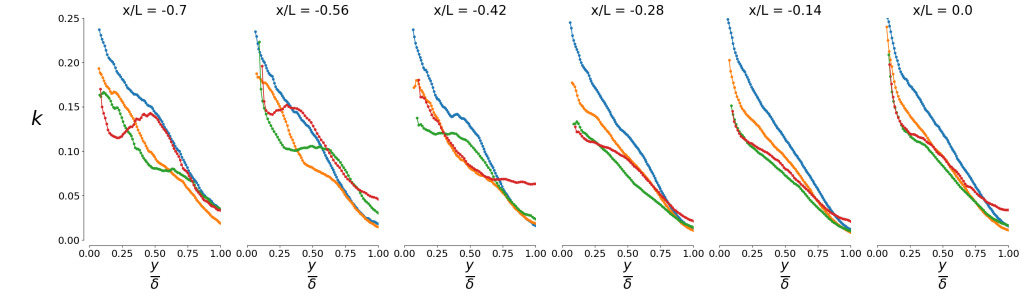

(d) Turbulent kinetic energy

Fig. 7 Reynolds stresses and turbulent kinetic energy in the FPG region of the flowfield. Legend in table 1

In summary, we observe some unique statistics in the upstream region of PG16 and PG21, both of which also have a different β_0 behavior in that region. We observe these two cases starting to saturate in terms of Reynolds stresses and TKE. PG8 on the other hand shows behavior consistent with both canonical FPG flows [4] and also bump type flows [19]. Based on these observations, we have developed a couple of hypotheses which we investigate and discuss in the upcoming subsections.

B. Relaminarization

The observations in the previous section, namely, the apparent collapse of PG16 and PG21 in figure 7a, suggest a saturation in the suppression by the two PGs, meaning that the boundary layer is not experiencing a significant reduction in turbulence production in PG21 compared to PG16. This points us to the possibility that the flow might be experiencing the onset of relaminarization, and thus, there is no significant difference in turbulence production between the two as seen in the TKE and RS profiles. This hypothesis is further supported by the fact that the acceleration parameter, K, for both of these cases, is higher than 3.7×10^{-6}, which according to Kline et al. [28] is the point at which they observe relaminarization. This is not a definitive criterion for verifying relaminarization but served as a preliminary check for our hypothesis. Note that from prior work in our research group in the APG region just downstream of this FPG region [22], we see evidence that the relaminarization process is not completed at $x/L = 0$ for any of the cases.

In terms of criteria, most criteria use inner-scaled parameters [7, 8, 12, 29] in order to determine this onset, which is not feasible due to lack of near-wall data. We can use estimations for near-wall quantities assuming ZPG quantities like the ones used by Narasimha and Sreenivasan [12], but these have been shown to be inaccurate [7]. It has been observed that the onset of relaminarization is coupled with a slight dip followed by a sharp increase in the shape factor, H [13, 30], which we can calculate using our data. This is also coupled with a drop in the displacement thickness, δ^*, which can be used as a secondary verification criterion.

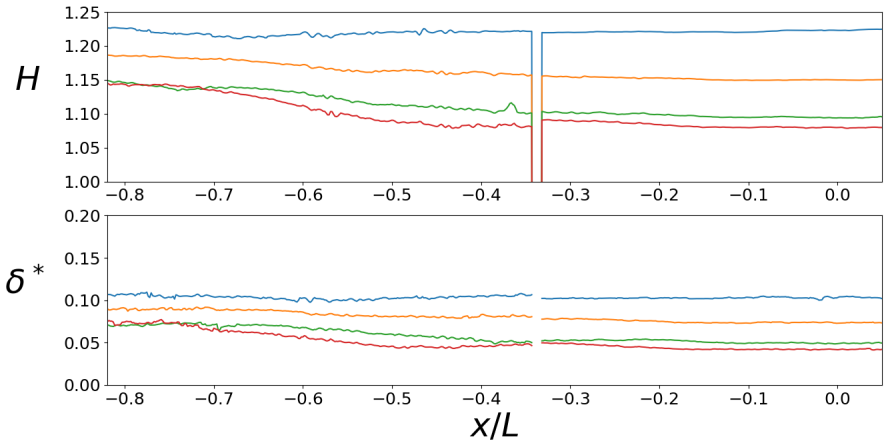

Fig. 8 Shape factor and displacement thickness in the FPG region of the flowfield. Legend in table 1

Figure 8 shows both H and δ^* for all four cases. Note that the missing data at $x/L \approx -0.33$ is a gap in the two camera's field of view, where we do not have data. We do see a dip in the shape factor plot for both PG16 and PG21 at $x/L \approx -0.38$ and $x/L \approx -0.45$, respectively. However, we never see the sharp increase expected for the onset of relaminarization, indicating that we do not have relaminarization. Looking at the PG distributions, PG16 dips below the $K = 3.7 \times 10^-6$ mark at $x/L \approx -0.64$ and PG21 at $x/L \approx -0.49$. So while the peak PG strength was strong enough to initiate relaminarization, it was not applied long enough to start the process. This explains why we start seeing the indication of possible relaminarization in the RS profiles and a dip in H, but we do not see relaminarization start. The δ^* plot supports this and does not show the drop expected for relaminarization.

C. Internal layer detection

Based on the observations of unusual behavior seen in section IV.A, as well as prior work with this flowfield by Parthasarathy and Saxton-Fox [22] showing the presence of internal layers in the APG region of this flowfield, we hypothesized the presence of internal layers within the FPG region as well. Following similar methodology to Parthasarathy and Saxton-Fox [22], we plot the mean velocity profiles against the root of y/δ, i.e., $\sqrt{y/\delta}$ vs. U/U_e. This is shown in figure 9. A distinct kink in this plot characterizes an internal layer, but a close inspection of this plot shows no obvious kinks that might indicate an internal layer.

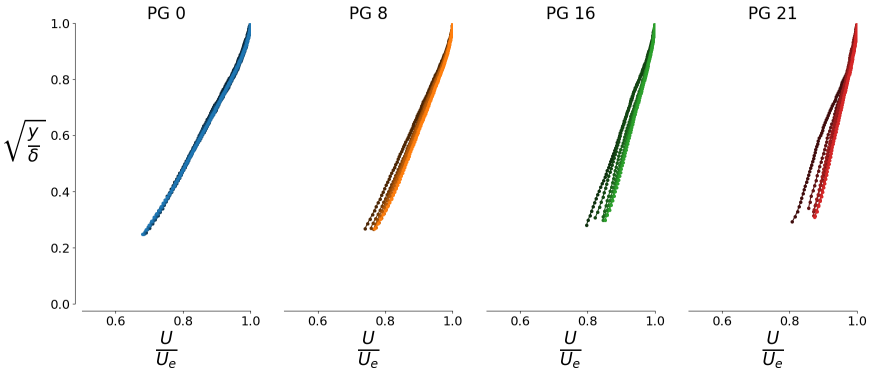

Fig. 9 velocity profile against the square root of y/δ. Suitable for locating internal layers. Legend in table 1

Note that bump flow literature has shown the presence of an internal layer starting at the beginning of the FPG region and another starting at the peak of the bump [19]. We expect this flowfield to show these same internal layers. As previously stated, the latter of the two has already been confirmed by Parthasarathy and Saxton-Fox [22]. As for the former, the unique behavior in the $\overline{u'u'}$ (figure 6a) showing a secondary peak (also called a knee point in literature) in the RS is consistent with the presence of an internal layer. However, that is not supported by figure 9. This may in fact be an internal layer, or something different. The secondary peak shows quick growth, which then remains relatively constant in strength and moves closer to the wall. The movement can be attributed to the FPG, but the growth rate for this peak is unexpectedly quick for an internal layer, especially considering the FPG, further weakening the argument for this being an internal layer.

While we see some phenomena in the Reynolds stresses which can be explained by internal layers, they show unusual behavior even for an internal layer. We also fail to detect a distinct internal layer boundary, which leads us to rule out an internal layer preliminarily.

V. Summary and Future Work

We performed an experimental study of the flow under a favorable-adverse pressure gradient sequence, which is a spatially varying pressure gradient imposing a favorable pressure gradient, starting at its strongest and gradually weakening, followed by an adverse pressure gradient starting at zero strength and increasing as the flow moves downstream. We tested this flowfield under 6 different pressure gradient strengths and at 6 different Reynolds numbers, of which 4 PGs are presented at $Re_\tau = 953$ in this work. We also present a new definition for a boundary layer edge which is based on the slope of the $\overline{u'v'}$ Renolds stress which goes to zero at the edge of the boundary layer. We found this definition to be more robust against experimental noise.

We observed the canonical FPG behavior for PG8, which involves a suppression of the Reynolds stresses and turbulent kinetic energy, a thinning of the boundary layer, as well as acceleration in the mean velocity profiles. The downstream portion of PG16 and PG21 ($x/L \geq -0.14$ and $x/L \geq -0.28$, respectively) also showed behavior consistent with an FPG TBL. PG0 presented with some behavior consistent with a weak FPG in the upstream region ($-0.7 \leq x/L \leq -0.56$), with the remaining consistent with a ZPG.

We also observed some unique behavior in the upstream parts of the stronger pressure gradients (PG16, PG21), which involved the growth of an outer peak (knee point) in the $\overline{u'u'}$ that stops growing at $x/L \approx -0.55$ and $x/L \leq -0.7$, respectively. This peak moves closer to the wall as the flow moves downstream, maintaining its strength after growth has concluded until it merges with the near-wall peak. These two pressure gradients show an increasing β_0 with increasing

x for the first third of the FPG region, which may be related to the qualitative difference in Reynolds stresses that we observe. We note that the x location at which the β_0 peaks does not correlate well with the x location at which the $\overline{u'u'}$ knee point / outer peak is at its strongest amplitude. After the outer peak merges with the near-wall peak, there is a dip (both PG16 and PG21) in the outer region along with an increase in the freestream $\overline{u'u'}$ for only the PG21 case. This $\overline{u'u'}$ behavior is mirrored by the TKE as well. We also see a rapid growth followed by immediate suppression in $\overline{u'v'}$ in the outer region. This growth occurs at $y/\delta \approx 0.5$ and $y/\delta \approx 0.35$ for PG16 and PG21, respectively, peaking at $x/L = -0.62$ and $x/L = -0.65$, respectively.

This unique behavior in Reynolds stresses was hypothesized to be caused by the presence of an internal layer, but the rapid growth in $\overline{u'u'}$ outer peak, combined with the lack of a distinct kink in the $\sqrt{y/\delta}$ vs. U/U_e profile, argues against this hypotheses. Future work will continue to investigate the source of the Reynolds stress behavior at the strongest pressure gradient strengths, including through the use of time-resolved data that we have acquired for the same field of view. The flow structures in the region showing unique behavior will be investigated.

Secondly, we observe a convergence in Reynolds stresses between PG16 and PG21, which could suggest the onset of relaminarization in either one or both of the strongest PG cases. This hypothesis was not supported by the shape factor, H, and displacement thickness, δ^*, with the former not showing the expected rapid rise and the latter not showing the expected dip. Based on this, we conclude that even for the strongest PG case we do not see relaminarization.

Acknowledgment

This material is based upon work supported by the Office of Naval Research Grant N00014-21-1-2648 and the National Science Foundation under Award No. 2339665

References

[1] Harun, Z., Monty, J. P., and Marusic, I., "The structure of zero, favorable and adverse pressure gradient boundary layers," *Begel House Inc.*, 2011. https://doi.org/10.1615/TSFP7.30.

[2] Dixit, S. A., and Ramesh, O. N., "Pressure-gradient-dependent logarithmic laws in sink flow turbulent boundary layers," *Journal of Fluid Mechanics*, Vol. 615, 2008, p. 445–475. https://doi.org/10.1017/S0022112008004047.

[3] Dixit, S. A., and Ramesh, O. N., "Large-scale structures in turbulent and reverse-transitional sink flow boundary layers," *Journal of Fluid Mechanics*, Vol. 649, 2010, p. 233–273. https://doi.org/10.1017/S0022112009993430.

[4] Volino, R. J., "Non-equilibrium development in turbulent boundary layers with changing pressure gradients," *Journal of Fluid Mechanics*, Vol. 897, 2020, p. A2. https://doi.org/10.1017/jfm.2020.319.

[5] Gungor, T. R., Maciel, Y., and Gungor, A. G., "Energy transfer mechanisms in adverse pressure gradient turbulent boundary layers: production and inter-component redistribution," *Journal of Fluid Mechanics*, Vol. 948, 2022, p. A5. https://doi.org/10.1017/jfm.2022.679.

[6] Vinuesa, R., Örlü, R., Sanmiguel Vila, C., Ianiro, A., Discetti, S., and Schlatter, P., "Revisiting History Effects in Adverse-Pressure-Gradient Turbulent Boundary Layers," *Flow Turbul. Combust.*, Vol. 99, No. 3, 2017, pp. 565–587. https://doi.org/10.1007/s10494-017-9845-7.

[7] BOURASSA, C., and THOMAS, F. O., "An experimental investigation of a highly accelerated turbulent boundary layer," *Journal of Fluid Mechanics*, Vol. 634, 2009, p. 359–404. https://doi.org/10.1017/S0022112009007289.

[8] Narayanan, M. A. B., and Ramjee, V., "On the criteria for reverse transition in a two-dimensional boundary layer flow," *Journal of Fluid Mechanics*, Vol. 35, No. 2, 1969, p. 225–241. https://doi.org/10.1017/S002211206900108X.

[9] Monty, J., Harun, Z., and Marusic, I., "A parametric study of adverse pressure gradient turbulent boundary layers," *International Journal of Heat and Fluid Flow*, Vol. 32, No. 3, 2011, pp. 575–585. https://doi.org/https://doi.org/10.1016/j.ijheatfluidflow.2011.03.004, URL https://www.sciencedirect.com/science/article/pii/S0142727X11000452, 8th International Symposium on Engineering Turbulence Modelling and Measurements, Marseille, France,June 9 to 11, 2010.

[10] Sanmiguel Vila, C., Örlü, R., Vinuesa, R., Schlatter, P., Ianiro, A., and Discetti, S., "Adverse-Pressure-Gradient Effects on Turbulent Boundary Layers: Statistics and Flow-Field Organization," *Flow Turbulence and Combustion*, Vol. 99, 2017, pp. 589–612. https://doi.org/10.1007/s10494-017-9869-z.

[11] Maciel, Y., Wei, T., Gungor, A. G., and Simens, M. P., "Outer scales and parameters of adverse-pressure-gradient turbulent boundary layers," *Journal of Fluid Mechanics*, Vol. 844, 2018, p. 5–35. https://doi.org/10.1017/jfm.2018.193.

[12] Narasimha, R., and Sreenivasan, K. R., "Relaminarization in highly accelerated turbulent boundary layers," *Journal of Fluid Mechanics*, Vol. 61, No. 3, 1973, p. 417–447. https://doi.org/10.1017/S0022112073000790.

[13] Ugo Piomelli †, E. B., and Pascarelli, A., "Turbulent structures in accelerating boundary layers," *Journal of Turbulence*, Vol. 1, 2000, p. N1. https://doi.org/10.1088/1468-5248/1/1/001, URL https://doi.org/10.1088/1468-5248/1/1/001.

[14] Hosseini, S., Vinuesa, R., Schlatter, P., Hanifi, A., and Henningson, D., "Direct numerical simulation of the flow around a wing section at moderate Reynolds number," *International Journal of Heat and Fluid Flow*, Vol. 61, 2016, pp. 117–128. https://doi.org/https://doi.org/10.1016/j.ijheatfluidflow.2016.02.001, URL https://www.sciencedirect.com/science/article/pii/S0142727X16300169, sI TSFP9 special issue.

[15] Lee, J.-H., and Sung, H. J., "Effects of an adverse pressure gradient on a turbulent boundary layer," *International Journal of Heat and Fluid Flow*, Vol. 29, No. 3, 2008, pp. 568–578. https://doi.org/https://doi.org/10.1016/j.ijheatfluidflow.2008.01.016, URL https://www.sciencedirect.com/science/article/pii/S0142727X0800012X, the Fifth International Symposium on Turbulence and Shear Flow Phenomena (TSFP5).

[16] Coleman, G. N., Rumsey, C. L., and Spalart, P. R., "Numerical study of turbulent separation bubbles with varying pressure gradient and Reynolds number," *Journal of Fluid Mechanics*, Vol. 847, 2018, p. 28–70. https://doi.org/10.1017/jfm.2018.257.

[17] Roidl, B., Meinke, M., and Schröder, W., "Boundary layers affected by different pressure gradients investigated computationally by a zonal RANS-LES method," *International Journal of Heat and Fluid Flow*, Vol. 45, 2014, pp. 1–13. https://doi.org/https://doi.org/10.1016/j.ijheatfluidflow.2013.11.004, URL https://www.sciencedirect.com/science/article/pii/S0142727X13002154.

[18] Ashton, N., West, A., Lardeau, S., and Revell, A., "Assessment of RANS and DES methods for realistic automotive models," *Computers & Fluids*, Vol. 128, 2016, pp. 1–15. https://doi.org/https://doi.org/10.1016/j.compfluid.2016.01.008, URL https://www.sciencedirect.com/science/article/pii/S0045793016000190.

[19] Balin, R., and Jansen, K., "Direct numerical simulation of a turbulent boundary layer over a bump with strong pressure gradients," *Journal of Fluid Mechanics*, Vol. 918, 2021, p. A14. https://doi.org/10.1017/jfm.2021.312.

[20] Shur, M. L., Spalart, P. R., Strelets, M. K., and Travin, A. K., "Direct numerical simulation of the two-dimensional speed bump flow at increasing Reynolds numbers," *International Journal of Heat and Fluid Flow*, Vol. 90, 2021, p. 108840. https://doi.org/https://doi.org/10.1016/j.ijheatfluidflow.2021.108840, URL https://www.sciencedirect.com/science/article/pii/S0142727X21000709.

[21] Uzun, A., and Malik, M., "Simulation of a turbulent flow subjected to favorable and adverse pressure gradients," *Theoretical and Computational Fluid Dynamics*, Vol. 35, 2021, pp. 1–37. https://doi.org/10.1007/s00162-020-00558-4.

[22] Parthasarathy, A., and Saxton-Fox, T., "A family of adverse pressure gradient turbulent boundary layers with upstream favourable pressure gradients," *Journal of Fluid Mechanics*, Vol. 966, 2023, p. A11. https://doi.org/10.1017/jfm.2023.429.

[23] Cavar, D., and Meyer, K. E., "Investigation of Turbulent Boundary Layer Flow Over 2D Bump Using Highly Resolved Large Eddy Simulation," *Journal of Fluids Engineering*, Vol. 133, No. 11, 2011, p. 111204. https://doi.org/10.1115/1.4005262, URL https://doi.org/10.1115/1.4005262.

[24] Webster, D. R., Degraaff, D. B., and Eaton, J. K., "Turbulence characteristics of a boundary layer over a two-dimensional bump," *Journal of Fluid Mechanics*, Vol. 320, 1996, p. 53–69. https://doi.org/10.1017/S0022112096007458.

[25] Parthasarathy, A., and Saxton-Fox, T., "A novel experimental facility to impose unsteady pressure gradients on turbulent boundary layers," *Experiments in Fluids*, Vol. 63, 2022. https://doi.org/10.1007/s00348-022-03456-z.

[26] Griffin, K. P., Fu, L., and Moin, P., "General method for determining the boundary layer thickness in nonequilibrium flows," *Phys. Rev. Fluids*, Vol. 6, 2021, p. 024608. https://doi.org/10.1103/PhysRevFluids.6.024608, URL https://link.aps.org/doi/10.1103/PhysRevFluids.6.024608.

[27] Uzun, A., and Malik, M. R., *Simulation of a Turbulent Flow Subjected to Favorable and Adverse Pressure Gradients*, 2020. https://doi.org/10.2514/6.2020-3061, URL https://arc.aiaa.org/doi/abs/10.2514/6.2020-3061.

[28] Kline, S. J., Reynolds, W. C., Schraub, F. A., and Runstadler, P. W., "The structure of turbulent boundary layers," *Journal of Fluid Mechanics*, Vol. 30, No. 4, 1967, p. 741–773. https://doi.org/10.1017/S0022112067001740.

[29] Patel, V. C., "Calibration of the Preston tube and limitations on its use in pressure gradients," *Journal of Fluid Mechanics*, Vol. 23, No. 1, 1965, p. 185–208. https://doi.org/10.1017/S0022112065001301.

[30] Launder, B. E., "Laminarization of the Turbulent Boundary Layer in a Severe Acceleration," *Journal of Applied Mechanics*, Vol. 31, No. 4, 1964, pp. 707–708. https://doi.org/10.1115/1.3629738, URL https://doi.org/10.1115/1.3629738.